Soft Matter

Electronic Supplementary Information

Thermogelation of Nanoemulsions Stabilized by a Commercial Pea Protein Isolate: High-Pressure Homogenization Defines Gel Strength

Damian Renggli,[a] and Patrick S. Doyle,*[a]

Contents

[a] *Department of Chemical Engineering, Massachusetts Institute of Technology, Cambridge, MA 02139, USA; E-mail: pdoyle@mit.edu*

1 Supporting videos

Confocal z-scan of a pristine PPI10 dispersion

Video S 1 shows a z-scan comprised of 92 slices of the pristine PPI10 dispersion presented in Fig. 2 of the manuscript. The video shows the composite images of the Nile blue (yellow, protein), Calcofluor-white (cyan, cell-wall debris), and Nile red (magenta, lipid phases) in the same color as in Fig. 2 of the manuscript.

Confocal z-scan of a PPI10-Oil20 nanoemulsion homogenized for 20 passes at 30 kpsi

Video S 2 shows a z-scan comprised of 40 slices of the PPI10-Oil20 nanoemulsion homogenized with $n = 20$ passes at $P = 30\,\text{kpsi}$ presented in Fig. 5 of the manuscript. The video shows the composite images of the Nile blue (yellow, protein), Calcofluor-white (cyan, cell-wall debris), and Nile red (magenta, lipid phases) in the same color as in Fig. 5 of the manuscript. The scale bar represents $1\,\mu\text{m}$.

2 DLS scattering angle

We tested the validity of using a 90° scattering angle by measuring a mixture of polystyrene (PS) microparticles with diameters of 0.1 μm (Polysciences Inc., D = 0.102 μm, SD = 0.01 μm, 2.6 % solid content) and 1.0 μm (Polysciences Inc., D = 0.1009 μm, SD = 0.019 μm, 2.68 % solid content). Our instrument allows for detection angle of 90° (conventional DLS configuration) and 15° (forward scattering). We prepared diluted 1:1 mixtures by volume and present averages of two samples per scattering angle with 5 consecutive measurements (2 min) after a 10 min calibration time at 25 °C in Fig. S 1. We used the second cumulant method because of the narrow size distribution of the PS particles. The forward scattering is clearly more sensitive to the large particles (1.0 μm indicated by the solid horizontal line) compared to the 90° configuration. However, the forward scattering configuration completely fails to detect the presence of the smaller particle population (0.1 μm indicated by the dashed horizontal line). We therefore validate the use of the conventional 90° scattering angle configuration.

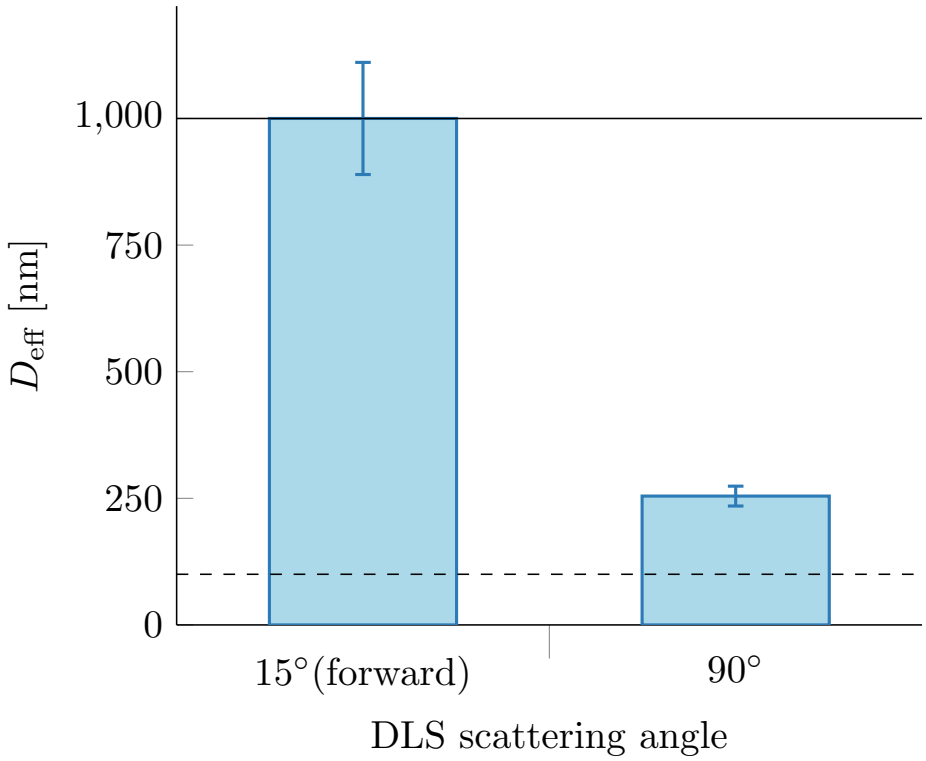

Fig. S 1 DLS of 1:1 mixtures of 0.1 μm and 1 μm polystyrene microparticles by volume performed at two different scattering angles and 25 °C. Each point is an average of five repetitions of two samples.

3 Surfactant to oil ratio

The surfactant-to-oil ratio (SOR) is useful to discuss the effect of varying PPI and oil content. Since the PPI is stabilizing the nanoemulsion droplets, a decrease in PPI leads to a strong increase of droplet diameter as shown in Fig. S 2A. Reducing the oil content accordingly hence keeping the SOR constant, very similar D_{eff} are achieved with the same processing. However, the reduced oil content results in a strong reduction of the resulting gel strength at 80 °C (see Fig. S 2B). In conclusion, the SOR defines the emulsion droplet size at the same processing parameters, and the oil volume fraction is responsible for the final gel strength after gelation.

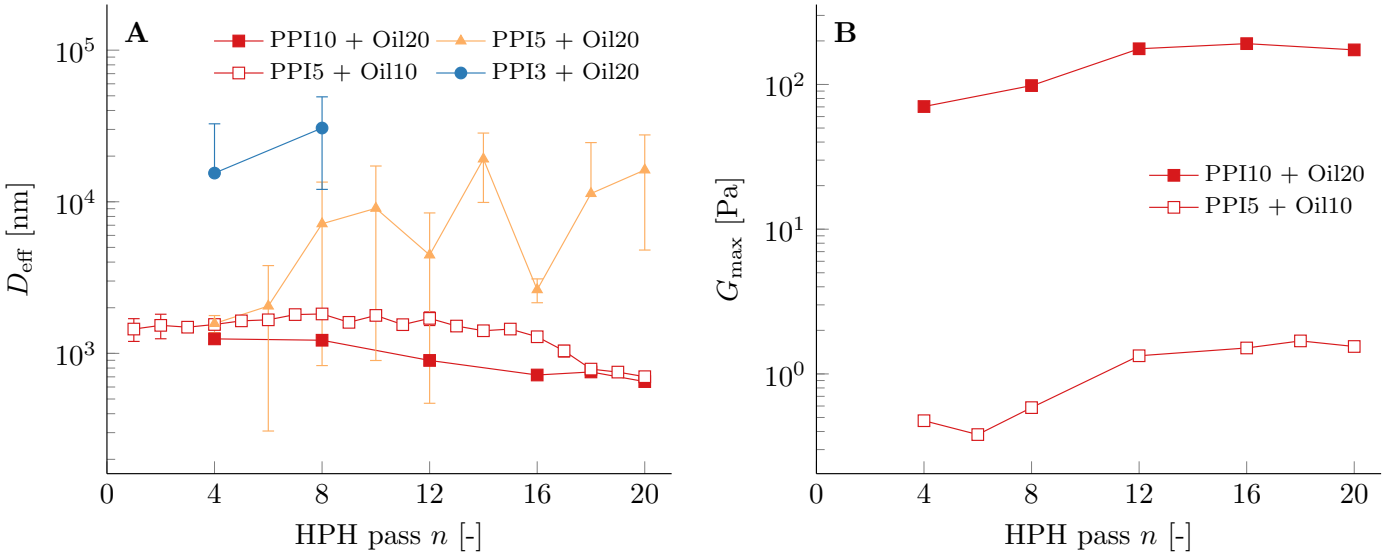

Fig. S 2 (A) Effective diameter and (B) maximum gel strength after gelation of nanoemulsions with composition defined by the legend. All nanoemulsions were prepared by processed PPI dispersions after $n = 4$ HPH passes. The rheology in (B) was measured with a 60 mm cone-plate geometry.

4 Bright-field and fluorescence microscopy images of PPI dispersions

A representative selection of bright-field and fluorescence confocal images of a 10 wt% PPI dispersion after $n = 1$ to 6 HPH passes at $P = 10$ kpsi is shown in Fig. S 3 according to Fig. 2 in the manuscript. In addition, an inverted composite is provided, where the black background has been inverted to white for better visibility of the lipid phase.

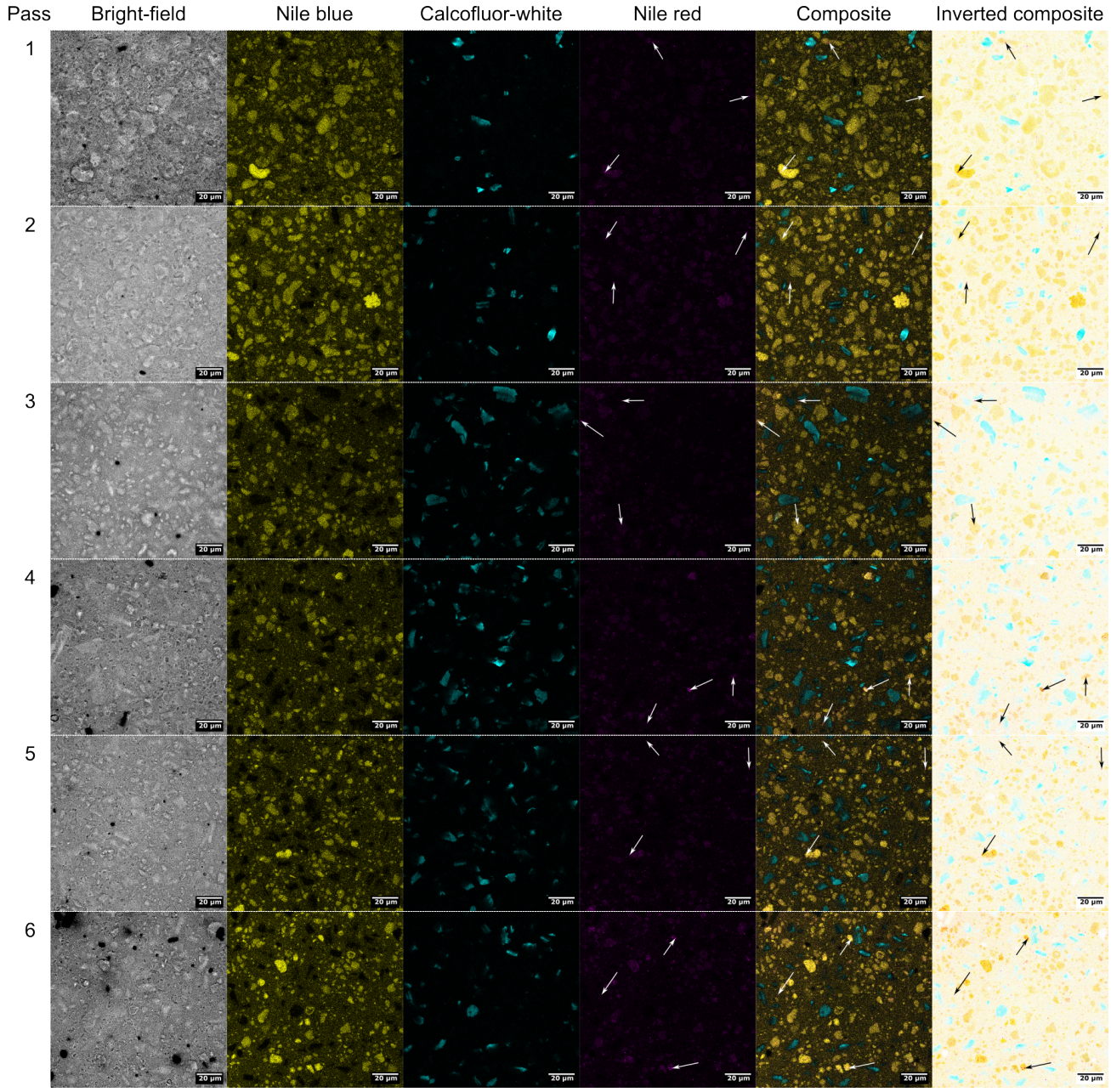

Fig. S 3 Bright-field and fluorescence confocal images of a 10 wt% PPI dispersion after $n = 1$ to 6 HPH passes at $P = 10$ kpsi. The black background has been inverted to white in the inverted composite image. Images recorded at room temperature and scale bar represents 20 μm.

5 Differential Scanning Calorimetry of PPI

Differential scanning calorimetry measurement of a PPI powder sample is shown in Fig. S 4A. Protein unfolding appears as endothermic signal, and the instrument software defines the peak at 66.10 °C and onset at 52.23 °C. Fig. S 4B shows the second heating cycle overlaid and the endothermic peak is absent. Furthermore, there is no peak visible in the cooling cycle in Fig. S 4C in between the two heating cycles. Hence the sample fully denatures during the first heating cycle.

The reported peak temperature is too low for reported denaturation temperatures of pea protein globulins[1–4]. However, a lipid phase transition such as melting or dehydration of polysaccharides should also be visible in the cooling cycle and also re-appear in the second heating cycle. In contrary, a protein unfolding is non-reversible, which is why we assigned the endothermic peak to protein unfolding. This does not have to correspond with the denaturation temperature of the native PPI protein, but it could represent the final unfolding of the already partially denatured pea proteins. The harsh extraction method usually leads to partial denaturation of the pea protein. A strongly reduced enthalpy has been observed for commercial PPI samples[1]. Furthermore, a shift to lower unfolding temperatures has been reported for misfolded states of lysozyme as a consequence of chemical pre-treatment[5].

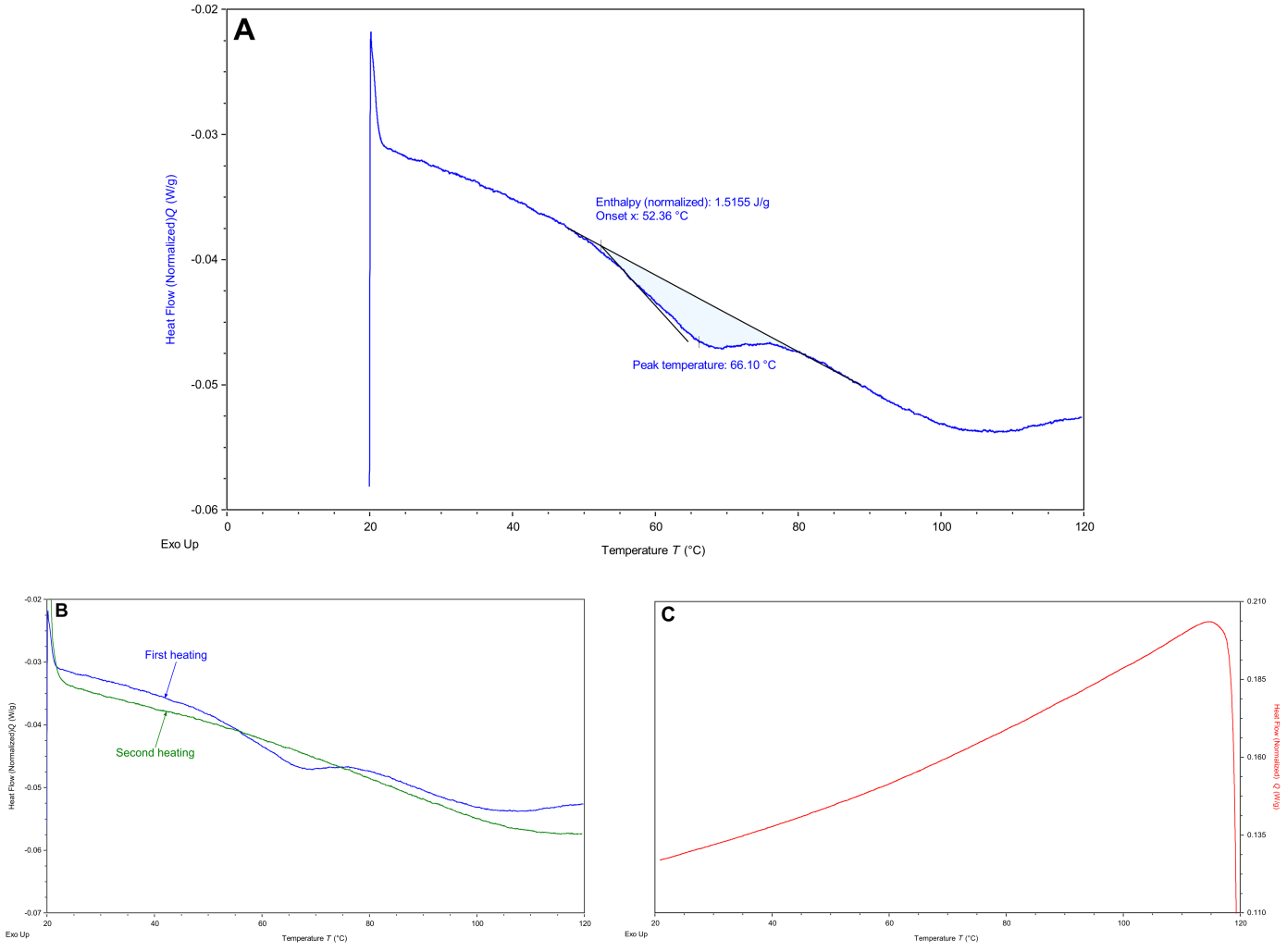

Fig. S 4 DSC of PPI powder with overlaid (A) analysis of the endothermal peak, (B) second heating cycle, and (C) cooling cycle. Heating and cooling rate is $2\,^{\circ}\mathrm{C\,min^{-1}}$ and $5\,^{\circ}\mathrm{C\,min^{-1}}$, respectively.

6 Effect of HPH on repeatability of PPI10 thermogelation behavior

Repetitions of the thermogelation experiment reveal a large variability between three individual pristine PPI10 samples, as shown in Fig. S 5. Only two of the three data sets extend into the time sweep at 80 °C (orange shaded area). On the one hand, the measured gel points ($\delta = 45°$) range from 58 °C to 77 °C and G' at 80 °C has a strong variability as direct consequence. On the other hand, the homogenized PPI10 dispersions show good repeatability and no gelation is observed even after equilibration at 80 °C for 10 min. The differences between the pristine and processed dispersions is most evident in the phase angle in Fig. S 5B. The small inconsistencies in G' when switching between the rheological tests persists because of reasons discussed earlier. We also measured repeated temperature ramps of pristine PPI10 samples that have been prepared from the same dispersion batch. Careful sample handling, where the temperature is kept below 4 °C at all times to avoid any thermal history, and constantly stirring of the batch to avoid sedimentation during the sample loading increases, but could not lead to a satisfactory repeatability of the pristine PPI10 samples (Fig. S 6). Evidently, the large insoluble PPI particles are an important constituent of the structure for the pristine sample. The measured dispersion properties are very sensitive on sample loading because of the non-Brownian behavior of these large particles and their sedimentation for the pristine dispersions.

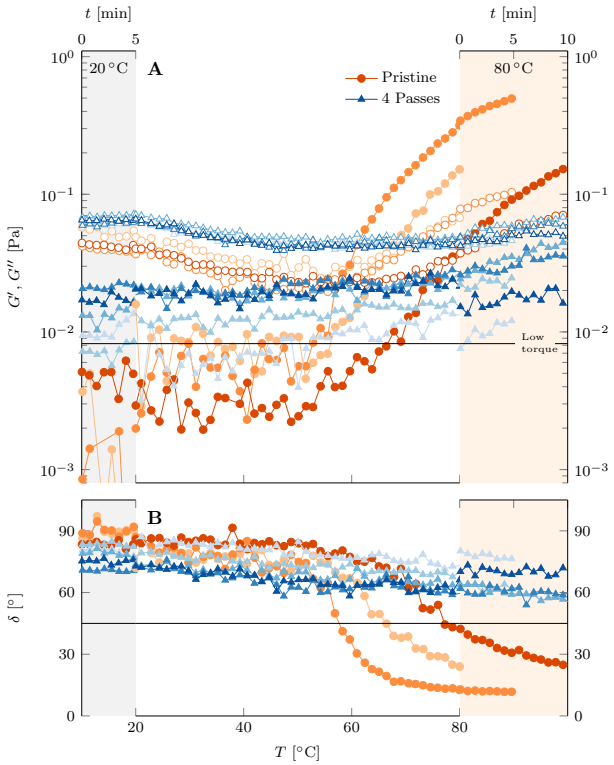

Fig. S 5 Repeatability of pristine $n = 0$ (circles) and homogenized $n = 4$ at $P = 10$ kpsi (triangles) 10 wt% PPI dispersions. (A) Full and empty symbols are storage modulus G' and loss modulus G'', respectively. Low torque limit is indicated by the solid horizontal line. (B) Phase angle. $\delta = 45°$ is indicated by the solid line. Equilibration time sweeps at 20 °C and 80 °C are shown in the preceding gray and subsequent orange shaded areas, respectively. Data measured at $f = 1$ Hz, $\gamma = 1$ %, and heating rate of 2 °C min^{-1}. Every tenth point shown for clarity.

Repetition of temperature sweeps from a large badge of pristine PPI10 dispersion

The repeatability of pristine PPI10 dispersions is investigated by performing temperature sweeps on samples from the same batch. Three batches are shown in Fig. S 6 where the sample was prepared with no environmental control (**A**), keeping $T \leq 4\,^{\circ}\mathrm{C}$ at all times (**B**), and keeping $T \leq 4\,^{\circ}\mathrm{C}$ at all times while stirring the dispersion batch. The repeatability is best for **C** but control remains weak.

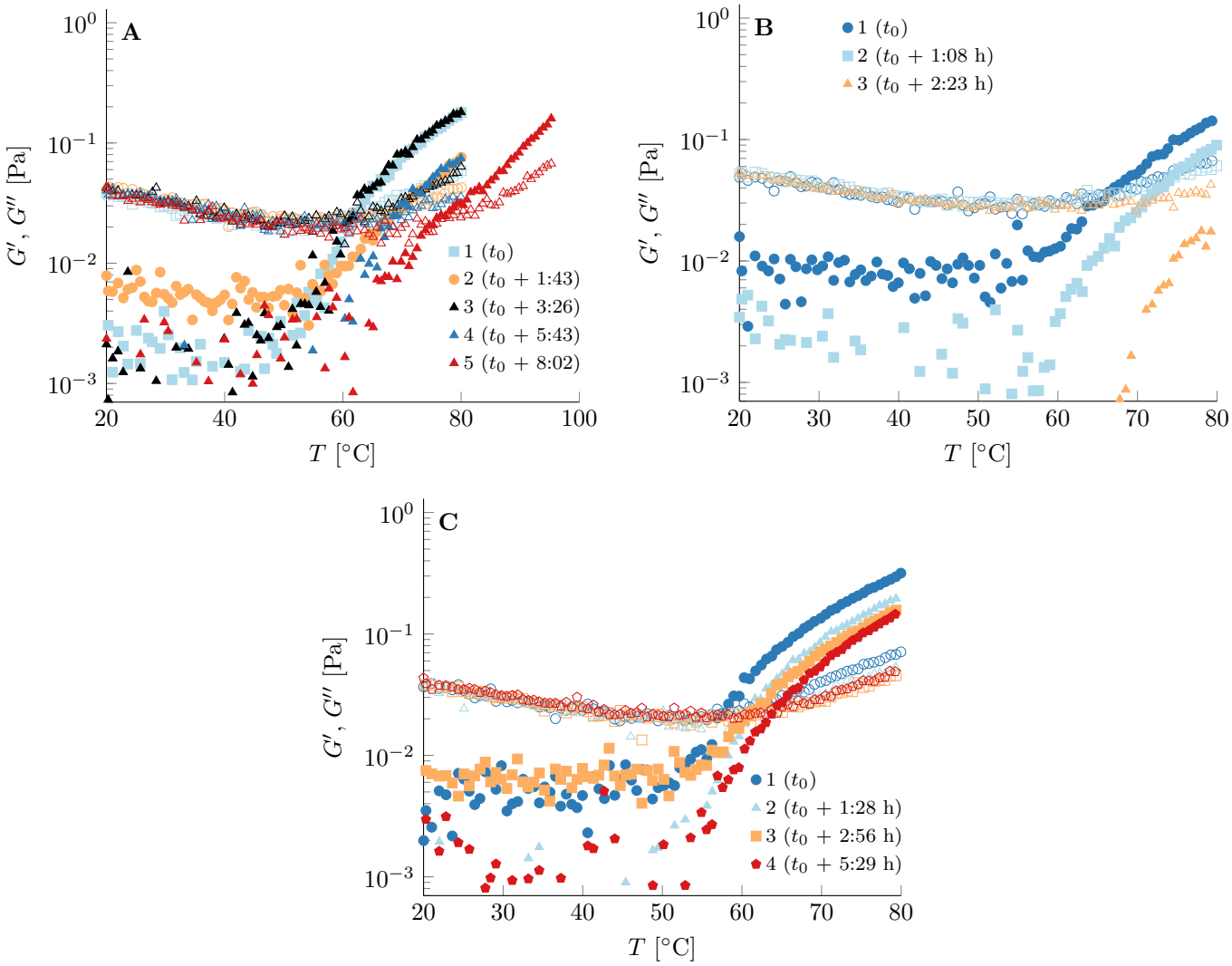

Fig. S 6 Temperature sweeps of pristine PPI10 dispersions with (A) no environmental control, (B) $T \leq 4\,^{\circ}\mathrm{C}$, and (C) $T \leq 4\,^{\circ}\mathrm{C}$ while stirring the dispersion batch. Open and closed symbols correspond to storage (G') and loss modulus (G''), respectively. The legend indicates the delay of a test with respect to the initial time of the first test t_0. Data measured at $f = 1\,\mathrm{Hz}$, $\gamma = 1\,\%$, and heating rate of $2\,^{\circ}\mathrm{C\,min^{-1}}$.

7 Cell-wall debris particle after 20 HPH passes at 30 kpsi of a PPI10-Oil20 nanoemulsion

Fluorescent confocal images of a PPI10-Oil20 nanoemulsion homogenized for $n = 20$ passes at $P = 30\,\mathrm{kpsi}$ are shown in Fig. S 7. A large cell-wall debris particle can easily be seen in the Calcofluor-white channel (Fig. S 7C). This demonstrates that the cell-wall debris particles are not efficiently broken down by the HPH processing at the highest pressure of $30\,\mathrm{kpsi}$.

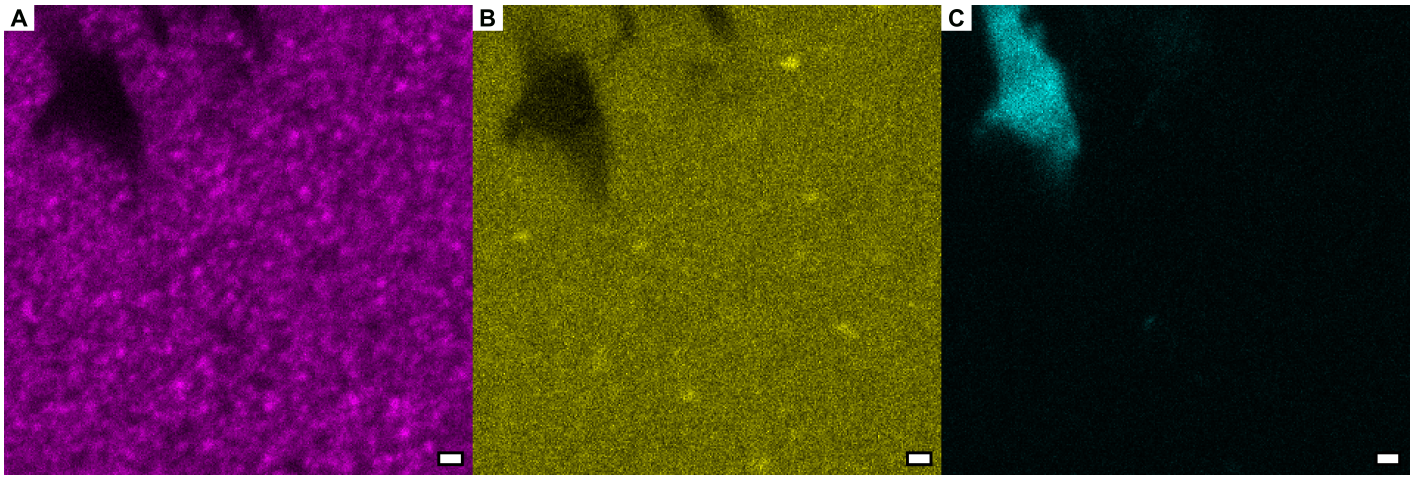

Fig. S 7 Fluorescence confocal images of a PPI10-Oil20(20) homogenized at $30\,\mathrm{kpsi}$ recorded at room temperature. (A) Nile red (lipid phase), (B) Nile blue (protein), and (C) Calcofluor-white (cell-wall debris) channel. Scale bar corresponds to $1\,\mu\mathrm{m}$.

8 Time-sensitivity of DLS experiments for PPI10-Oil20 nanoemulsions

Data of repeated DLS experiment of a PPI10-Oil20 nanoemulsion homogenized at 10 kpsi is shown in Fig. S 8. The repetition includes a fresh dilution of the nanoemulsion sample and is not the repeated measurement of the identical DLS cuvette. The nanoemulsion is stored at 4 °C in between repetitions. The time delay between processing and measurement of the initial sample (blue circles) is not minimized in the presented image. This is the reason for the larger D_{eff} values compared to the data presented in Fig. 7 of the manuscript.

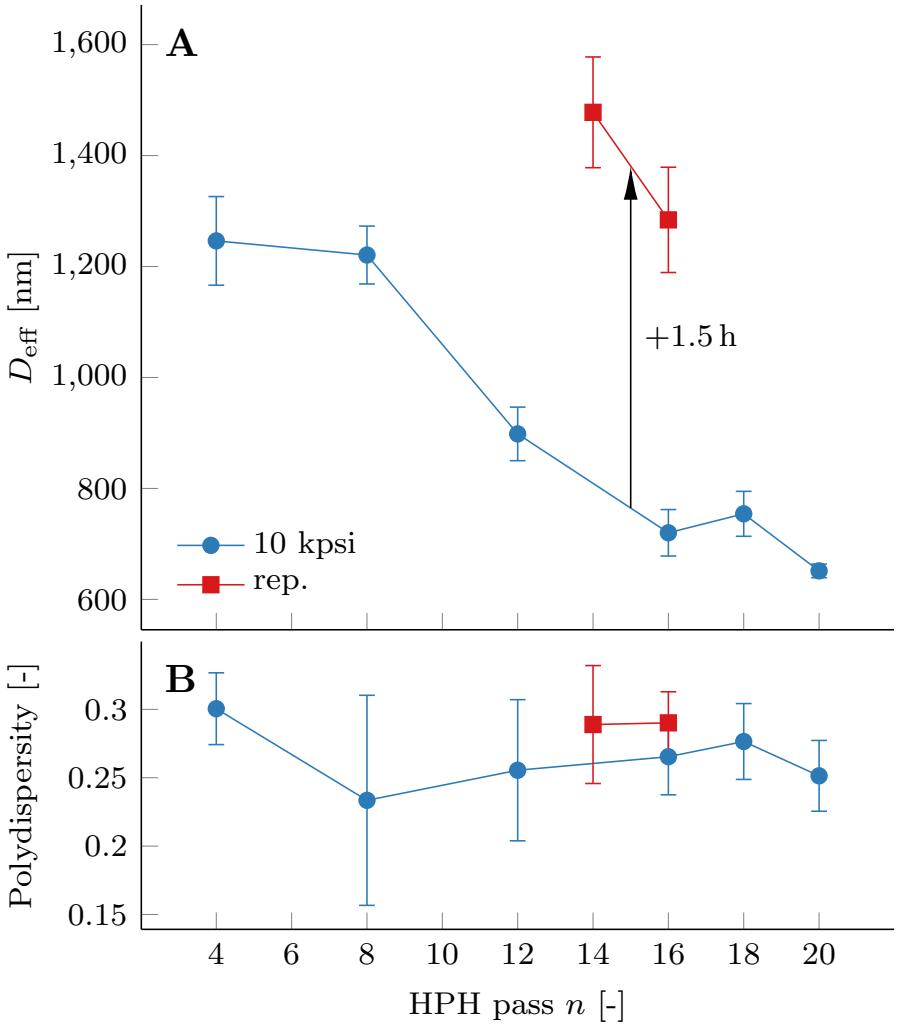

Fig. S 8 (A) Effective diameter and (B) polydispersity of 10 wt% PPI + 20 vol% oil nanoemulsions after $n = 4$ to 20 consecutive HPH passes at $P = 10$ kpsi. Square symbols show repeated measurements of the same sample with a delay of 1.5 h. Error bars correspond to standard deviations of at least 9 measurements. Measurements performed at 25 °C.

9 DLS analysis method

The DLS data presented in Fig. 7 & 11 of the manuscript are analysed with the CONTIN method and presented as comparison to the more robust second cumulant method used in the manuscript (see Fig. S 9). The CONTIN method is known to be suitable for polydisperse droplet distributions, and leads to slightly larger mean diameters compared to the the second cumulant method (D_{eff}). However, the reported trends are identical, but the CONTIN method leads to larger standard deviations of the same consecutive measurements hence the second cumulant method appears to lead to more stable results for our samples. The resulting power law exponent in Fig. S 9C is smaller compared to Fig. 11. However, the exponent is still larger than the scaling of interfacial area with droplet size (D_{eff}^{-2}). Fig. S 9 demonstrates that our findings are only marginally affected by the analysis method of the DLS data.

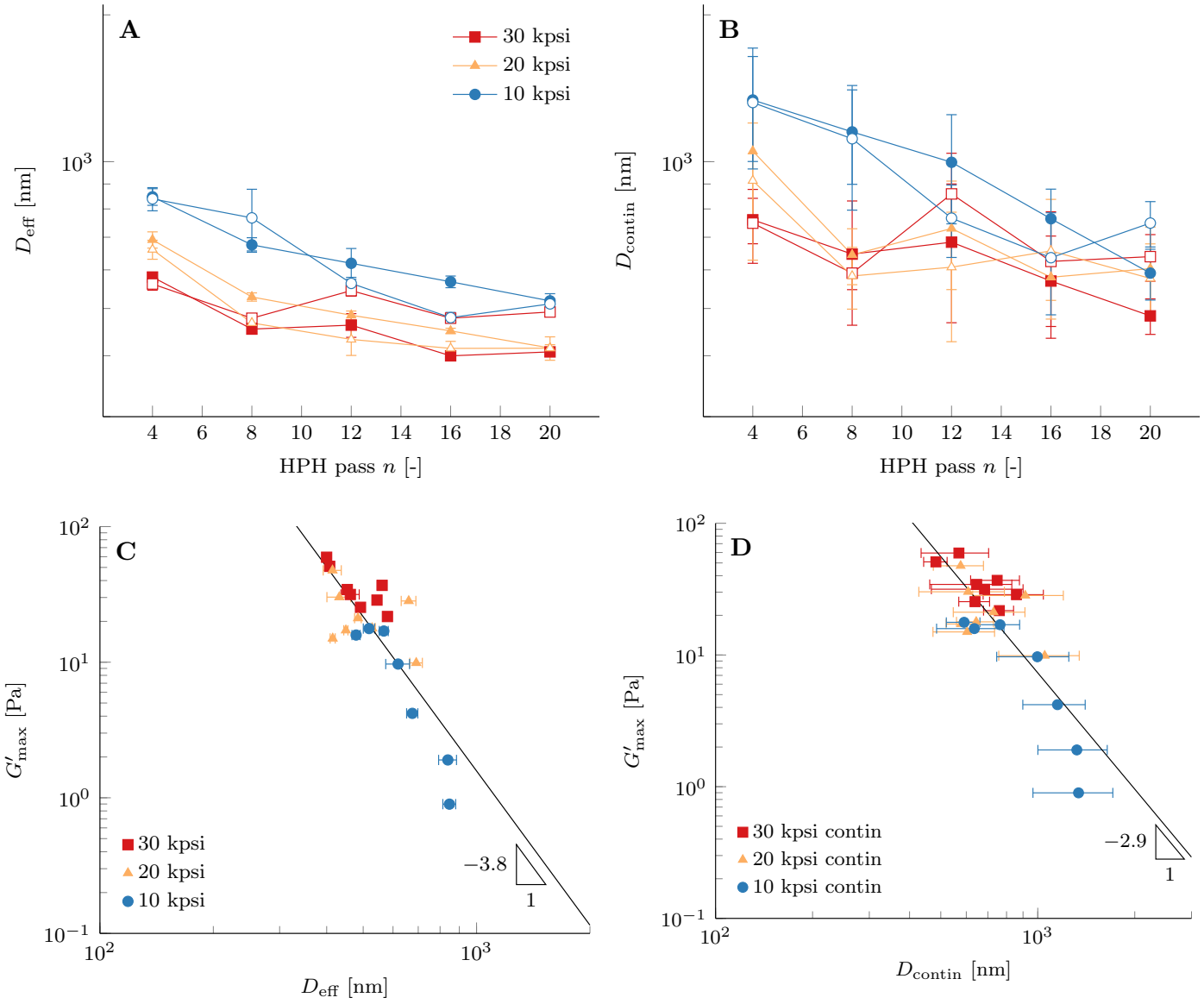

Fig. S 9 (A) Effective diameter resulting from second cumulant method and (B) mean diameter resulting from CONTIN method of the data presented in Fig. 7 of the manuscript. (C) Effective diameter resulting from second cumulant method with a power law fit with exponent of -3.8 ± 1.2 (95 % confidence interval) as a guide to the eye, and (D) mean diameter resulting from CONTIN method with a power law fit with exponent of -2.9 ± 0.9 (95 % confidence interval) as a guide to the eye of the data presented in Fig. 11 of the manuscript. We note that the data for effective diameter does not span a full decade and so fits to power-laws should be interpreted with caution.

10 Effect of sonication on PPI10 dispersions

We present DLS and thermogelation experiments on a PPI10 dispersion after $n = 4$ HPH passes at 10 kpsi in Fig. S 10. The effective particle diameter is slightly reduced by sonication. However, the standard deviations increase slightly, and the polydispersity does not seem to be affected. Furthermore, we did not observe any influence of sonication time on the thermogelation behavior of the sonicated PPI 10 dispersion. Therefore, the potential additional protein aggregate breakup during sonication resulting in a decreasing effective particle diameter has no effect on the thermogelation properties of the PPI10 dispersion after $n = 4$ HPH passes at 10 kpsi.

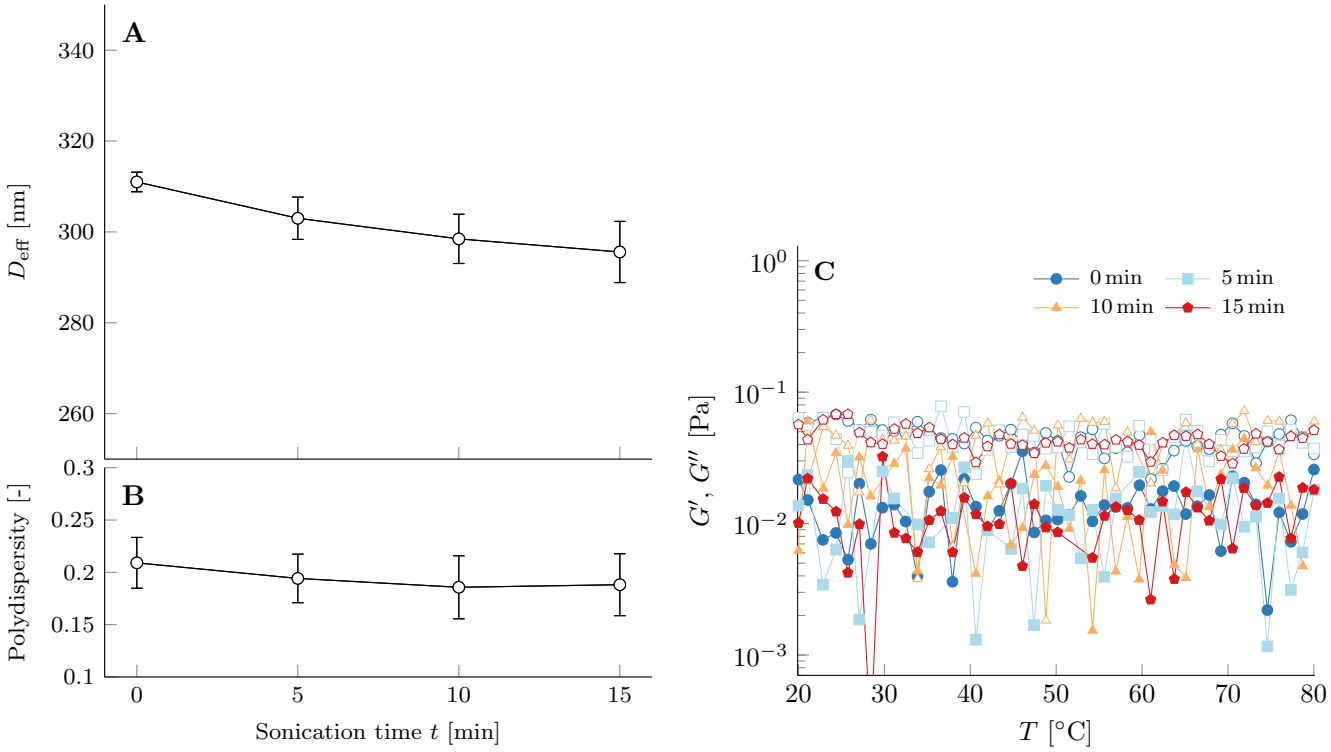

Fig. S 10 DLS experiment showing (A) effective diameter and (B) polydispersity, and rheological temperature sweep (C) of a 10 wt% PPI dispersion after $n = 4$ HPH passes at 10 kpsi as a function of sonication time t. Same parameters used as described in the manuscript. Only every 10th point shown in (C) for clarity.

11 Repeatability of PPI10-Oil20 thermogelation behavior

The repeatability of homogenized PPI10-Oil20 nanoemulsions is shown by two independently processed nanoemulsion samples undergoing thermogelation. The comparison is shown in Fig. S 11 where the HPH pressure P is set to 10 kpsi (**A**), 20 kpsi (**B**), and 30 kpsi (**C**).

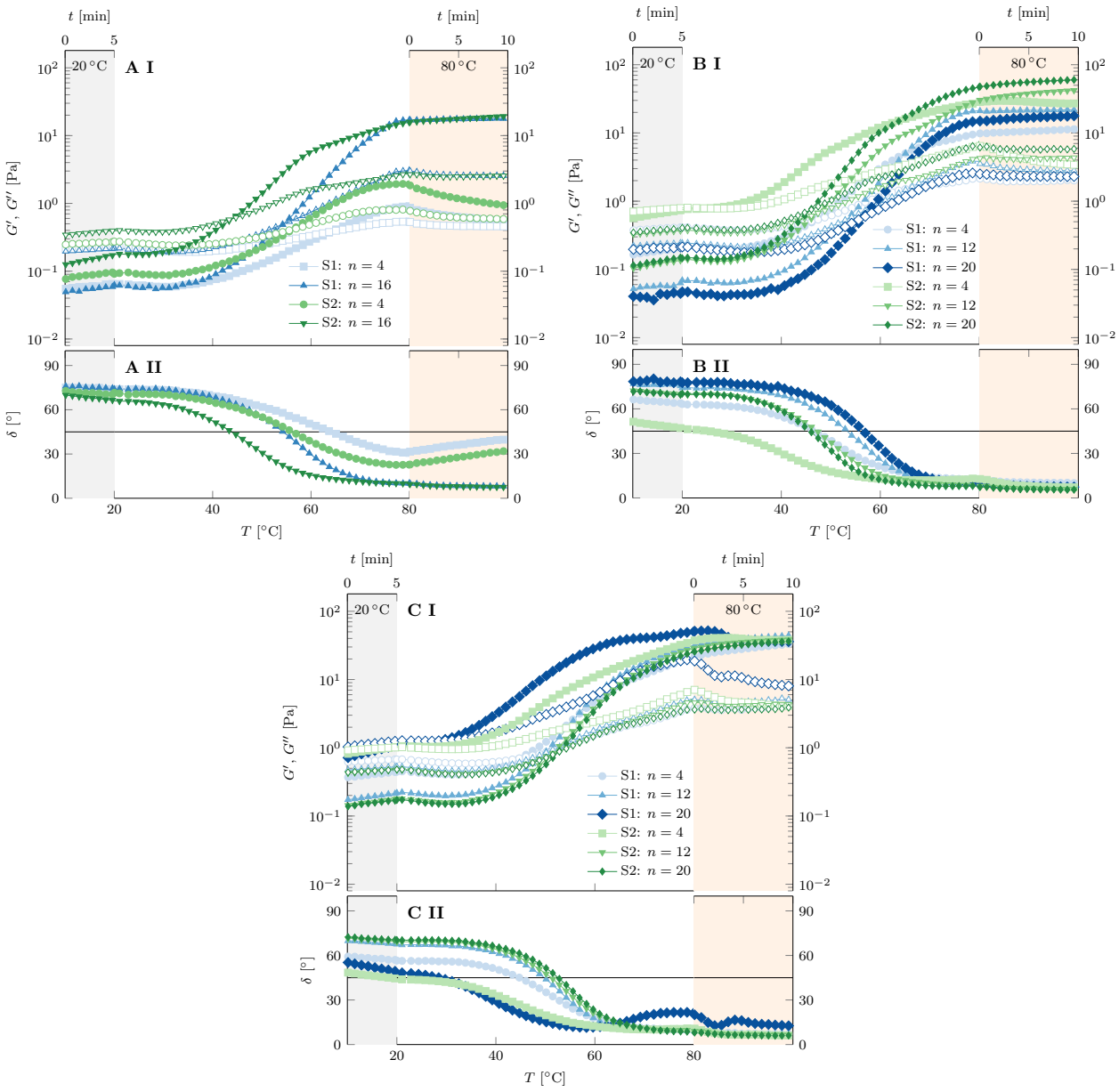

Fig. S 11 Repeated thermogelation data of independent PPI10-Oil20 nanoemulsions (samples S1 & S2) with (A) $P = 10\,\text{kpsi}$, (B) $P = 20\,\text{kpsi}$, and (C) $P = 30\,\text{kpsi}$. Open and closed symbols correspond to storage (G') and loss modulus (G''), respectively. The legend indicates the number of HPH passes n. Same experimental parameters as the data presented in the manuscript.

12 Frequency sweeps and strain amplitude sweeps of all emulsion samples after gelation — instrument inertia

The frequency sweeps and strain amplitude sweeps at 80 °C after gelation of all nanoemulsion samples are shown in Fig S. 12 for HPH pressure of 10 kpsi, Fig S. 13 for HPH pressure of 20 kpsi, and Fig S. 14 for HPH pressure of 30 kpsi.

All three images show (**A** & **D**) Frequency sweep, (**B** & **E**) applied strain amplitude sweep, and (**C** & **F**) resulting stress amplitude sweep of 10 wt% PPI + 20 vol% oil nanoemulsions at 80 °C. The legend shows the number of HPH passes. (**A**-**C**) Full and empty symbols are storage modulus G' and loss modulus G'', respectively. (**D**-**F**) Phase angle δ. $\delta = 45°$ is indicated by the solid line. The solid line in (**A**) indicates the contribution of instrument inertia with inertia constant $I = 25.3\,\mu\mathrm{N\,m\,s^2}$ measured during instrument calibration[6]. Data measured at frequency of 1 Hz and shear strain amplitude of 1 %, if not stated otherwise.

The inset in (**D**) shows the raw phase angle prior to instrument inertia correction. The correction allows for accurate measurements beyond the solid line in (**A**), but becomes unreliable for raw phase angle values larger than 175°[7].

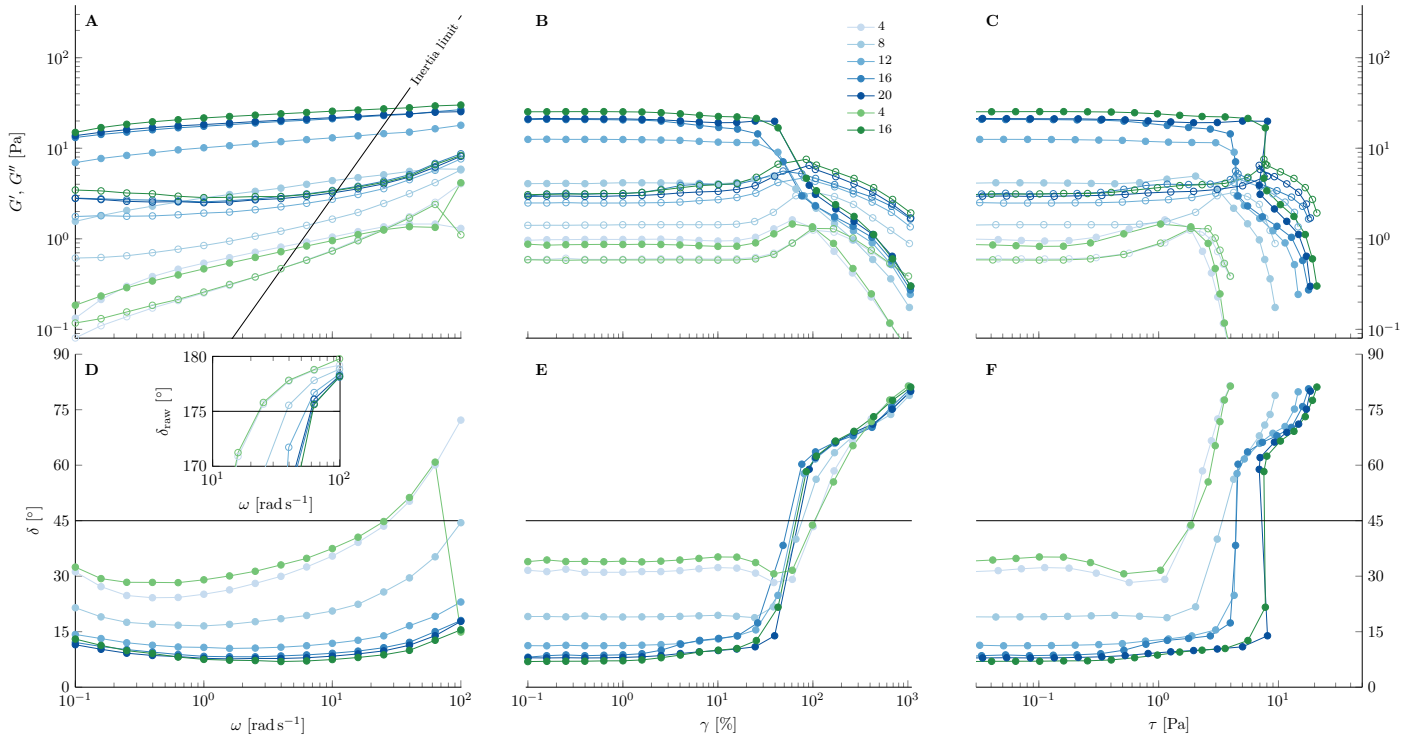

Fig. S 12 Rheological tests of 10 wt% PPI + 20 vol% oil nanoemulsions homogenized at 10 kpsi at 80 °C. The legend shows the number of HPH passes.

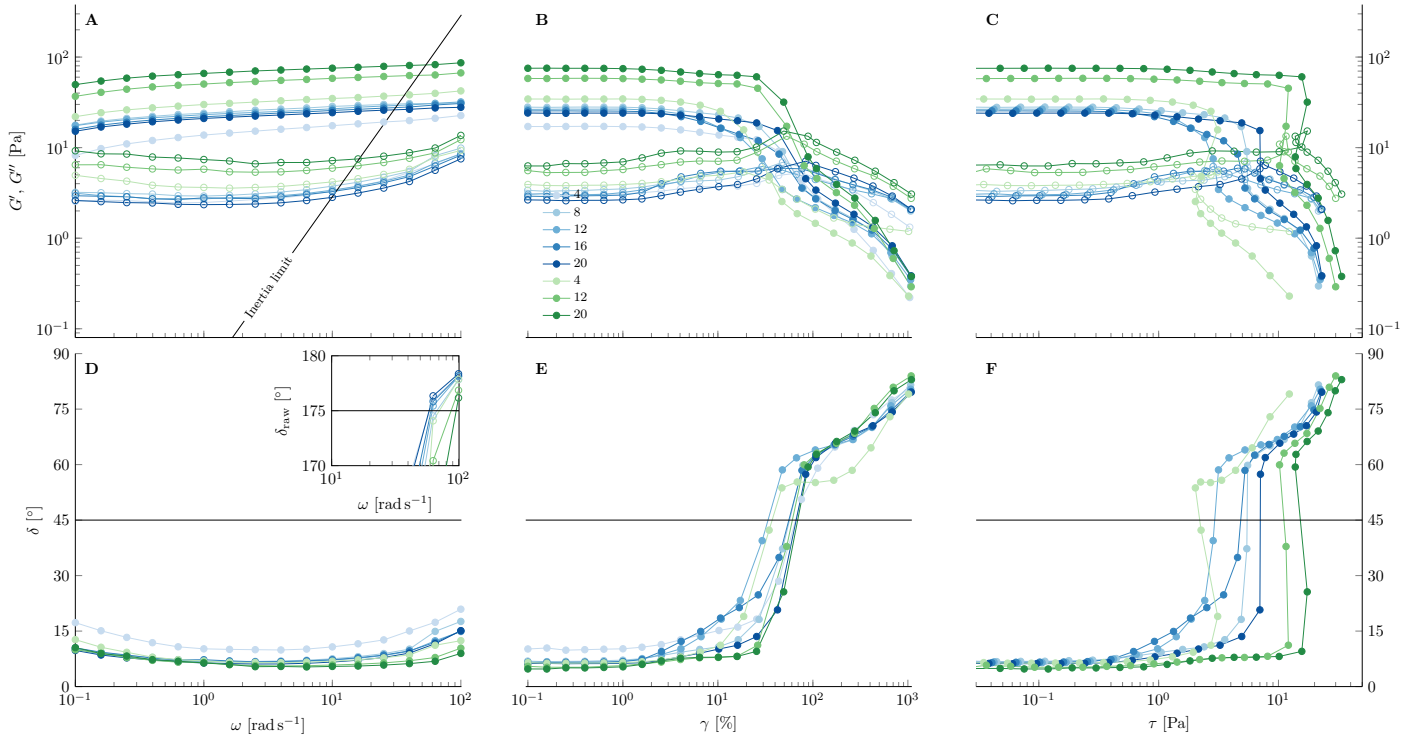

Fig. S 13 Rheological tests of 10 wt% PPI + 20 vol% oil nanoemulsions homogenized at 20 kpsi at 80 °C. The legend shows the number of HPH passes.

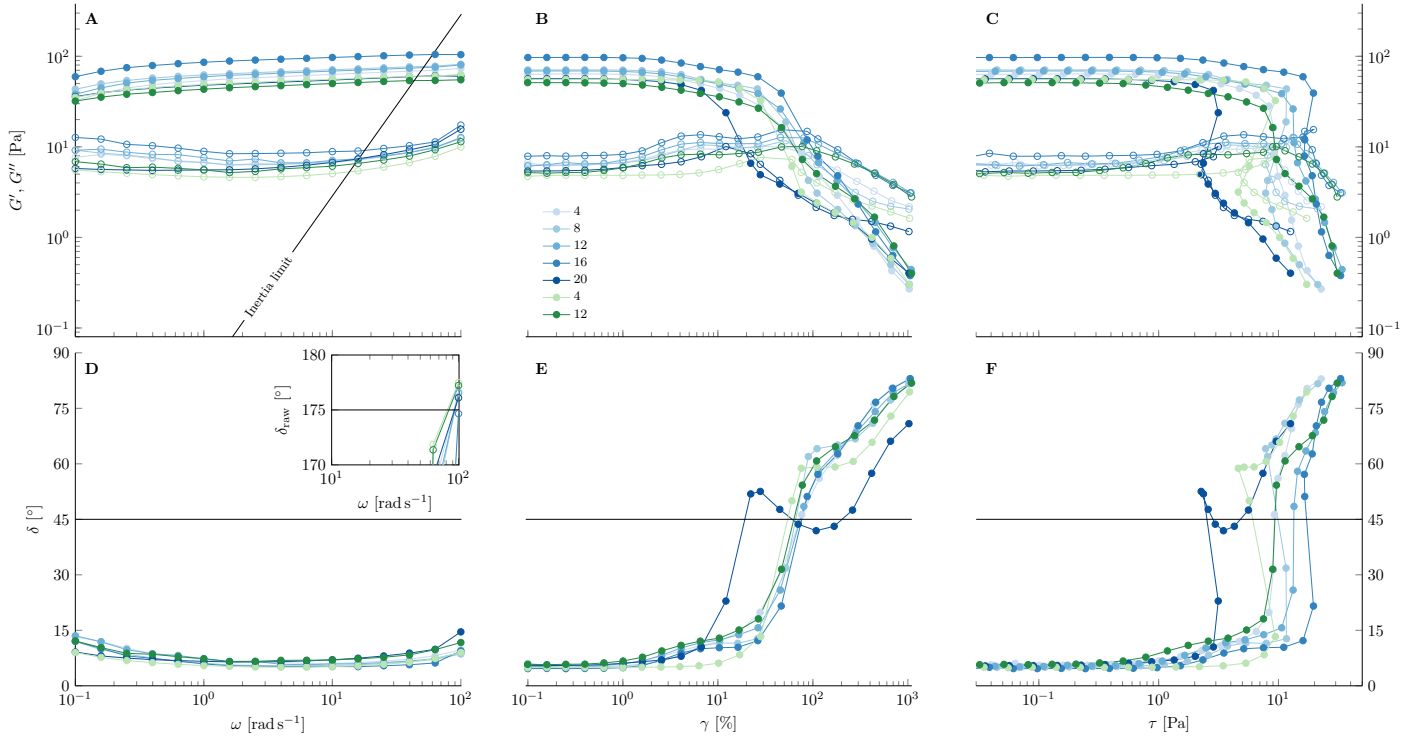

Fig. S 14 Rheological tests of 10 wt% PPI + 20 vol% oil nanoemulsions homogenized at 30 kpsi at 80 °C. The legend shows the number of HPH passes.

13 Stress amplitude–strain amplitude curve

The resulting stress amplitude τ is shown as a function of the strain amplitude γ in Fig. S 15. The abrupt change in resulting stress upon yielding can lead to a non-equidistant log-spaced strain amplitude value because a stress controlled rheometer is used for the measurements and the feedback loop for the strain-controlled mode is not fast enough to accommodate for the change.

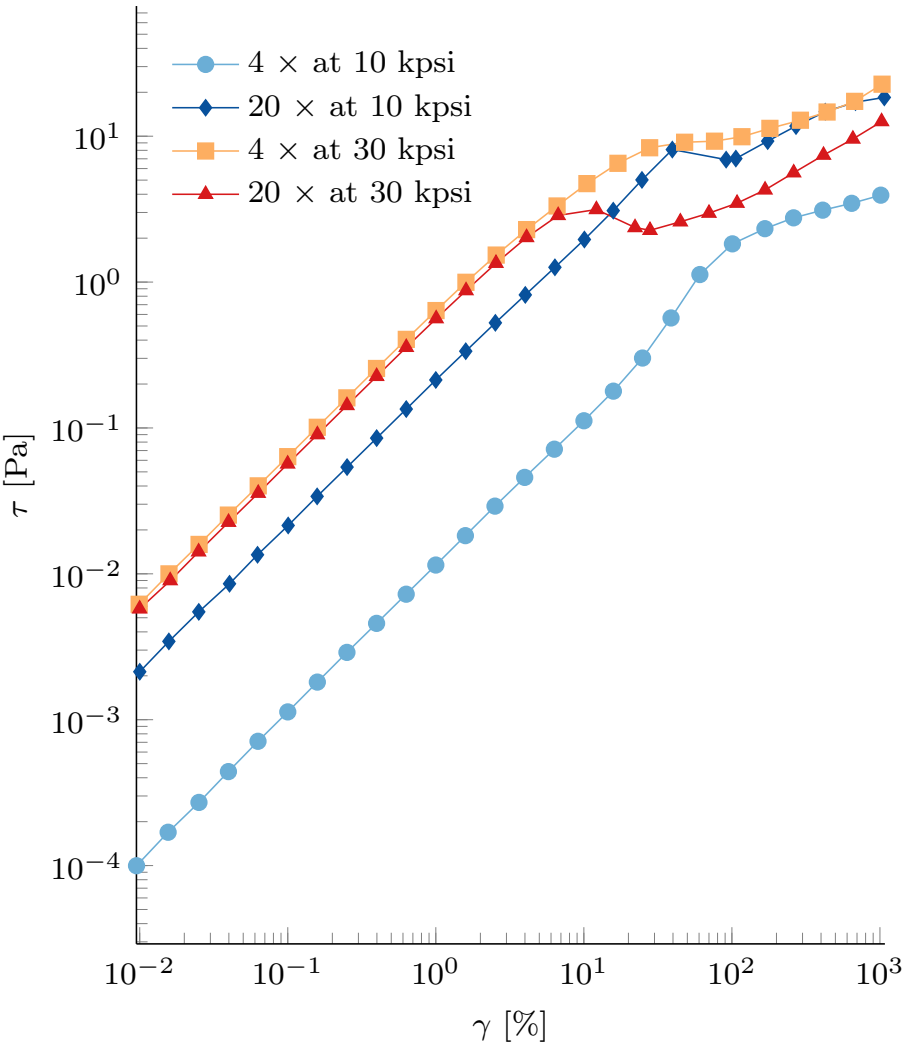

Fig. S 15 Stress amplitude as a function of strain amplitude for the strain amplitude sweep data shown in Fig. 13.

References

1 X. D. Sun and S. D. Arntfield, *Food Research International*, 2010, **43**, 509–515.

2 J.-L. Mession, N. Sok, A. Assifaoui and R. Saurel, *Journal of Agricultural and Food Chemistry*, 2013, **61**, 1196–1204.

3 J.-L. Mession, M. L. Chihi, N. Sok and R. Saurel, *Food Hydrocolloids*, 2015, **46**, 233–243.

4 C. Tanger, M. Müller, D. Andlinger and U. Kulozik, *Food Hydrocolloids*, 2022, **123**, 106903.

5 A. Cooper, *The Journal of Physical Chemistry Letters*, 2010, **1**, 3298–3304.

6 R. H. Ewoldt, M. T. Johnston and L. M. Caretta, in *Experimental Challenges of Shear Rheology: How to Avoid Bad Data*, Springer New York, 2014, pp. 207–241.

7 D. Renggli, A. Alicke, R. H. Ewoldt and J. Vermant, *Journal of Rheology*, 2020, **64**, 141–160.